SEDIMENTOLOGY the journal of the International Association of Sedimentologists

Sedimentology (2017) **64**, 186–203 doi: 10.1111/sed.12303

A Southern Hemisphere record of global trace-metal drawdown and orbital modulation of organic-matter burial across the Cenomanian–Turonian boundary (Ocean Drilling Program Site 1138, Kerguelen Plateau)

ALEXANDER J. DICKSON*, MATTHEW SAKER-CLARK*, HUGH C. JENKYNS*, CINZIA BOTTINI†, ELISABETTA ERBA†, FABIO RUSSO†, OLGA GORBANENKO*‡, BERNHARD D. A. NAAFS§, RICHARD D. PANCOST§, STUART A. ROBINSON*, SANDER H.J.M VAN DEN BOORN¶ and ERDEM IDIZ*¶

**Department of Earth Sciences, University of Oxford, South Parks Road, Oxford, OX1 3AN, UK (E-mail: alex.dickson@earth.ox.ac.uk)*

†Department of Earth Sciences, Università degli Studi di Milano, 20133 Milan, Italy

‡Department of Geosciences, Universität Tübingen, Hölderlinstrasse 12, 72074, Tübingen, Germany

§Organic Geochemistry Unit, Cabot Institute and School of Chemistry, University of Bristol, Cantock's Close, Bristol, BS8 1TS, UK

¶Shell Projects and Technology, Kessler Park 1, 2288 GS Rijswijk, The Netherlands

Associate Editor – Ulrich Heimhofer

ABSTRACT

Despite its assumed global nature, there are very few detailed stratigraphic records of the late Cenomanian to the early Turonian Oceanic Anoxic Event 2 from the Southern Hemisphere. A highly resolved record of environmental changes across the Cenomanian–Turonian boundary interval is presented from Ocean Drilling Program Site 1138 on the central Kerguelen Plateau (southern Indian Ocean). The new data lead to three key observations. Firstly, detailed biostratigraphy and chemostratigraphy indicate that the record of Oceanic Anoxic Event 2 is not complete, with a hiatus spanning the onset of the event. A decrease in glauconite and highly weathered clays after the onset of Oceanic Anoxic Event 2 marks the end of the hiatus interval, which can be explained by a relative sea-level rise that increased sediment accommodation space on the Kerguelen Plateau margin. This change in depositional environment controlled the timing of the delayed peak in organic-matter burial during Oceanic Anoxic Event 2 at Site 1138 compared with other Oceanic Anoxic Event 2 locations worldwide. A second key observation is the presence of cyclic fluctuations in the quantity and composition of organic matter being buried on the central Kerguelen Plateau throughout the latter stages of Oceanic Anoxic Event 2 and the early Turonian. A close correspondence between organic matter, sedimentary elemental compositions and sediments recording sea-floor oxygenation suggests that the cycles were mainly productivity-driven phenomena. Available age-control points constrain the periodicity of the coupled changes in sedimentary parameters to *ca* 20 to 70 ka, suggesting a link between carbon burial and astronomically forced climatic variations (precession or obliquity) in the Southern Hemisphere mid-latitudes both during, and after, Oceanic Anoxic Event 2: fluctuations that were superimposed on the impact of global-scale processes. Finally, trace-metal data from the black-shale unit at Site 1138 provide the first evidence from outside of the proto-North Atlantic region for a global drawdown of

seawater trace-metal (Mo) inventories during Oceanic Anoxic Event 2.

Keywords Kerguelen Plateau, molybdenum isotopes, Oceanic Anoxic Event 2, orbital forcing, organic-matter burial, sea-level change, trace metals.

INTRODUCTION

The environmental systems on Earth are related in a complex and often non-linear fashion. Globally significant perturbations in climate, such as those that occurred throughout the Mesozoic (Jenkyns, 2003), produce a diverse array of sedimentary responses, because they are filtered through a host of local-scale to regional-scale sedimentary controls such as basin geometry, temperature, hydrological cycling, weathering rates, rock-types, biotic community composition, relative sea-level and nutrient dynamics, among others. During Oceanic Anoxic Event 2 (OAE-2), a large increase in organic-carbon burial at a global scale led to a positive carbon-isotope excursion (CIE) that can be used as a chemostratigraphic marker for the event in lithologically diverse sedimentary successions (Scholle & Arthur, 1980; Tsikos *et al.*, 2004). However, even in well-studied regions, such as the proto-North Atlantic region and Western Interior Seaway of North America, the timing of organic-carbon accumulation and environmental change at a local scale does not always mirror the accompanying global carbon-isotope shift (e.g. Meyers *et al.*, 2001; Jenkyns, 2010; Eldrett *et al.*, 2014). Thus, the presence of a C-isotope excursion at any given location does not allow the direct extrapolation of global-scale climatic phenomena to that region.

Many hypotheses have been presented to account for increases in the global rate of organic-carbon burial during OAE-2. Possible mechanisms include eustatic sea-level rise that moved oxygen minimum zones onto the continental shelf (Schlanger & Jenkyns, 1976; Arthur *et al.*, 1987; Gavrilov *et al.*, 2013), an increase in the delivery of weathering-derived nutrients to the oceans (Frijia & Parente, 2008; Pogge van Strandmann *et al.*, 2013; Monteiro *et al.*, 2012; Blättler *et al.*, 2011), the input of volcanically derived nutrients to the oceans (Kerr, 1998; Larson & Erba, 1999; Turgeon & Creaser, 2008; Du Vivier *et al.*, 2014), changes in the cycling of major nutrients (Mort *et al.*, 2007; Adams *et al.*, 2010; Higgins *et al.*, 2012) and an expansion of sea-floor anoxia that inhibited carbon remineralization (Owens *et al.*, 2013; Westermann *et al.*, 2014). A global expansion of sea-floor anoxia has been most readily identified from the trace-metal abundances and isotopic signatures of proto-North Atlantic sedimentary deposits (e.g. Hetzel *et al.*, 2009; Westermann *et al.*, 2014). However, the proto-North Atlantic Ocean had a palaeoceanographic configuration that was unique in Late Cretaceous time for being affected by a high degree of hydrographic restriction, which might have induced basin-scale artifacts into trace-metal data.

The vast majority of the evidence underpinning hypotheses of carbon burial and environmental change during OAE-2 has been generated from the North Atlantic–Tethyan region (e.g. Kolonic *et al.*, 2005; Turgeon & Brumsack, 2006; Parente *et al.*, 2008; Turgeon & Creaser, 2008; Voigt *et al.*, 2008; Owens *et al.*, 2013; van Bentum *et al.*, 2012; Du Vivier *et al.*, 2014; Eldrett *et al.*, 2014; Lenniger *et al.*, 2014; van Helmond *et al.*, 2014; Westermann *et al.*, 2014). Consequently, it is unclear whether many of these hypotheses are relevant for locations outside of this region. The lack of data from the Southern Hemisphere also limits the potential to validate model simulations of environmental processes, such as the presence of sea-floor anoxia (total oxygen depletion) and euxinia (anoxia and the presence of H_2S in seawater), which has been argued to have occupied large areas of the sea floor during OAE-2 (e.g. Monteiro *et al.*, 2012).

This study addresses the Southern Hemisphere data 'gap' by generating new, multi-proxy records of the environmental changes spanning the late Cenomanian–early Turonian interval recorded from Ocean Drilling Program (ODP) Site 1138 on the central Kerguelen Plateau (Indian Ocean). Firstly, new nannofossil and carbon-isotope chemostratigraphic data are used to establish a high-precision (centimetre-scale) stratigraphic interpretation of the sedimentary succession at Site 1138 that was not possible with the existing lower resolution data from the core (Holbourn & Kuhnt, 2002; Meyers *et al.*, 2009). Secondly, the work of Meyers *et al.* (2009) is built upon by using new geochemical and petrographic data to interpret the changes

in depositional environment recorded at Site 1138, to characterize the type of organic matter being buried on the Kerguelan Plateau, and to evaluate the timing of organic-matter burial relative to other OAE-2 successions worldwide. Lastly, trace-metal data are used to test the hypothesis of a global drawdown in seawater inventories (specifically Mo) for the first time from a location outside of the hydrographically restricted proto-North Atlantic Ocean.

SITE DESCRIPTION

The Kerguelen Plateau is a submarine large igneous province (LIP) that was formed mostly during the early part of the Cretaceous Period (Frey *et al.*, 2000). Argon–Argon dating of basalts underlying marine sediments of Cretaceous age has shown that most of the central and southern portions of the Plateau were emplaced during eruptive phases older than *ca* 100 Ma (Frey *et al.*, 2000; Duncan, 2002). However, in Cretaceous times, portions of the Plateau were subaerially exposed, as illustrated by the presence of pahoehoe lavas and pyroclastic flows interbedded with shallow-marine sediments in drill cores from ODP Leg 183 (Frey *et al.*, 2000). At some sites, sediments containing terrestrially derived organic matter (for example, wood fragments and seeds) directly overlie the youngest lavas, indicating the presence of exposed land immediately after the major phase of Early Cretaceous volcanism (Mohr *et al.*, 2002; Meyers *et al.*, 2009). Site 1138 is located at 53·5°S, at a latitude that has remained the same since the Early Cretaceous (Shipboard Scientific Party, 2000) (Fig. 1). The sedimentary succession at Site 1138 records a transition from shallow-marine to deeper marine deposits throughout the Late Cretaceous, and its present-day water depth is *ca* 1400 m. (Shipboard Scientific Party, 2000; Meyers *et al.*, 2009).

METHODS

Samples spanning the upper Cenomanian–lower Turonian were taken from the archive half of ODP Site 1138, core 69, at 5 cm intervals. Aliquots of each sample were used for nannofossil biostratigraphy, organic geochemistry and inorganic geochemistry.

Nannofossil biostratigraphy

Semi-quantitative analyses of calcareous nannofossils were performed on a total of 50 smear-slides using standard light microscope techniques under cross-polarized and transmitted light, at 1250× magnification. At least two traverses of each smear-slide were investigated. Smear-slides were prepared following the methodology described by Monechi & Thierstein (1985). A small amount of rock material was powdered into a mortar with few drops of bi-distilled water and placed onto a glass coverslip. Using a toothpick, the suspension was repeatedly smeared along the coverslip to achieve the required thickness of smear, this being subsequently dried on a hotplate. The coverslip was

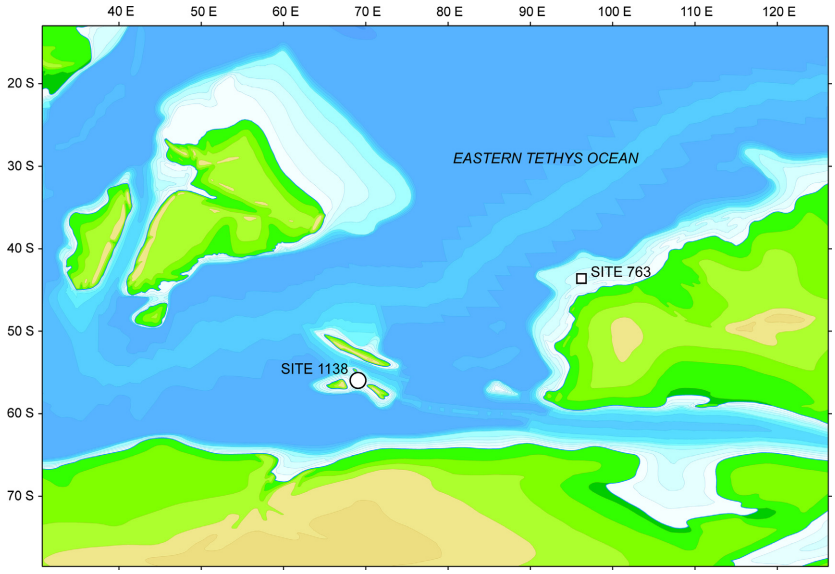

Fig. 1. MERLIN+ palaeogeography of the southern Tethys Ocean during the Cenomanian–Turonian boundary interval (*ca* 92 Ma). The location of ODP Site 1138 on the central Kerguelen Plateau is marked with a circle symbol. Additional Cenomanian–Turonian boundary locations in the region are marked with open square symbols. Projection is reproduced courtesy of Jim Harris, CGG Robertson, Merlin+ Project, 2015.

mounted onto the glass slide with Norland Optical Adhesive, and glued by exposure to UV light for a few minutes. The taxonomic concepts for calcareous nannofossil species identification follow the original descriptions and the discussions by Perch-Nielsen (1985), Burnett (1998) and Lees (2007). The nannofossil zonations used here for the Cenomanian–Turonian interval were adopted from Gambacorta *et al.* (2015).

Organic geochemistry

Total carbon (TC) and total inorganic-carbon (TIC) abundances were measured from *ca* 200 mg powder aliquots using a Ströhlein Coulomat device. Total inorganic-carbon (TIC) samples were analysed after removing organic carbon by furnacing overnight at 450°C. Total organic carbon (TOC) abundances were calculated by subtracting TIC from TC. The $\%CaCO_3$ abundances were calculated by multiplying TIC by 8·33 (molar proportion of C in $CaCO_3$); *ca* 1 g powder aliquots were prepared for bulk organic-carbon-isotope ($\delta^{13}C_{TOC}$) analysis by decarbonating twice in 1 M HCl, followed by rinsing three times in de-ionized water. Enough decarbonated powder was weighed into tin capsules to obtain *ca* 100 μg organic carbon per analysis. Samples were analysed for $\delta^{13}C_{TOC}$ following combustion at 1100°C on a Europa Geo 20-20 mass spectrometer (MS; Sercon Limited, Crewe, UK) and are expressed relative to Vienna Pee Dee Belemnite (VPDB). Reproducibility was estimated from repeated measurements of an in-house alanine standard as ±0·08‰ [1 Standard Deviation (SD), $n = 45$]. The bulk organic-carbon characteristics [hydrogen index (HI), oxygen index (OI) and T_{MAX}] of the Site 1138 samples were further investigated by analysing *ca* 50 mg powder aliquots with a Rock-Eval 6 (Vinci Technologies SA, Nanterre, France; Behar *et al.*, 2001).

For biomarker analyses, *ca* 6 g powdered sample was ultrasonically extracted using methanol, then dichloromethane (DCM)/methanol (1 : 1, v/v) and, finally, 100% DCM. All extracts were combined and dried under N_2 at 40°C. Water was removed from the samples by passing the extracts [dissolved in DCM/methanol (3 : 1, v/v)] over a column containing anhydrous Na_2SO_4. The apolar fraction was obtained by passing the total lipid extract through a column containing activated Al_2O_3 using hexane/DCM (9 : 1, v/v). The apolar fraction was measured for compound-specific $\delta^{13}C$ using an Isoprime 100 GC-combustion-isotope ratio MS (GC-C-IRMS; Isoprime Limited, Stockport, UK) system at the Organic Geochemistry Unit, University of Bristol. To obtain enough organic matter for compound-specific $\delta^{13}C$ from organic-lean intervals [for example, >656·9 mbsf (metres below sea floor)], up to five samples were combined. Samples were measured in duplicate and $\delta^{13}C$ values were converted to VPDB by bracketing with CO_2 of known $\delta^{13}C$. The reported values are the average of the duplicate measurements. Instrument stability was monitored by regular analysis of an in-house fatty acid methyl ester standard mixture; long-term precision is ±0·3‰. After injection of 1 or 2 μl onto a Zebron-I non-polar column (50 m length × 0·32 mm diameter × 0·10 μm film thickness), the GC oven program was: 70°C (hold for 1 min) to 130°C at 20°C min^{-1}, then to 300°C at 4°C min^{-1} and hold for 25 min. Samples were automatically integrated using the IonVantage software package.

Organic petrography

For maceral analysis, chipped rock pieces were embedded in epoxy resin and prepared as polished sections. These sections were investigated using a Leica DMRX MPVSP microscope photometer (Leica Microsystems, Wetzlar, Germany) in both reflected white light and fluorescent mode under oil immersion at a magnification of 500×. The relative abundances of macerals, mineral groundmass and minerals were determined using a semi-automatic point counter. The maceral analysis is based on 1000 counts distributed regularly on the whole polished section. The nomenclature of the macerals of vitrinite and inertinite groups is based on Taylor *et al.* (1998), and the nomenclature of liptinite groups is based on Hutton (1987).

Inorganic geochemistry

Element abundances were measured by digesting 50 mg sample aliquots in a mixture of concentrated HNO_3/HCl/HF acids. Sample solutions were evaporated to dryness and re-dissolved in 2% HNO_3 at *ca* 5000-fold dilutions for trace-element analysis and *ca* 500 000-fold dilutions for major-element analysis. Measurements were made using a Perkin-Elmer quadrupole ICP-MS (Perkin Elmer, Waltham, MA, USA). Precision (2 SD) and accuracy were assessed by repeat digestions of USGS (United States Geological Survey) Devonian Shale SDO-1, and were both better than

±10% for Al, Mg, Na, Fe, Li, Mn, Mo and U. Results are expressed as enrichment factors [EF = $(element/Al)_{sample}/(element/Al)_{UCC}$], where upper continental-crust (UCC) abundances were taken from Rudnick & Gao (2003). Molybdenum isotopes were measured by adding a precise mass of a ^{100}Mo-enriched and ^{97}Mo-enriched double-isotope spike to sample aliquots containing *ca* 400 ng of natural Mo. The samples were digested in inverse aqua regia at 150°C for 48 h to ensure spike–sample equilibration, before purification of Mo using anion-exchange chromatography (Dickson *et al.*, 2016). Isotope ratios were measured using a Nu Plasma MC-ICP-MS (Nu Instruments Limited, Wrexham, UK) and are expressed as $\delta^{98/95}Mo = ((({}^{98/95}Mo_{sample} - {}^{98/95}Mo_{standard})/{}^{98/95}Mo_{standard})*1000)$ relative to NIST 3134 (Nägler *et al.*, 2014). External reproducibility was calculated by repeatedly processing aliquots of USGS SDO-1 shale through the full chemical and analytical procedure and was ±0·08‰ (2 SD, $n = 26$).

RESULTS

Nannofossil biostratigraphy

Moderately to well-preserved nannofossils are present in all samples apart from two barren intervals between 656·64 to 656·04 mbsf and 655·89 to 655·81 mbsf. Key marker events corresponding to the upper Cenomanian–lower Turonian interval were recognized as follows. Highest occurrences (HO) of *Corollithion kennedyi* and *Axopodorhabdus albianus* were observed at 656·89 mbsf and *Microstaurus chiastius* at 656·69 mbsf. Lowest occurrences (LO) of *Eprolithus octopetalus, Quadrum gartneri* and *Eprolithus eptapetalus* were identified at 655·99 mbsf, 655·75 mbsf and 655·47 mbsf, respectively (Figs 2 and 3; Table 1). Based on bio-events, zones and subzones were determined following the calcareous nannofossil biozonations of Sissingh (1977) implemented by Perch-Nielsen (1985), Bralower *et al.* (1995), Burnett (1998), Tsikos *et al.* (2004) and Gambacorta *et al.* (2015). The studied interval covers zones CC10 to CC11 of Sissingh (1977), zones NC11* to NC13* of Bralower *et al.* (1995), zones UC3a-c to UC7 of Burnett (1998), and zones NC11* to NC13** of Tsikos *et al.* (2004). The interval between 656·89 m and the top of the studied section is characterized by nannofossil events that provide a continuous zonation without evidence of hiatuses.

Organic geochemistry

The $\delta^{13}C_{TOC}$ fluctuates between *ca* −25·5‰ and −27‰ for the majority of the record (Figs 2 and 3), with transient positive and negative excursions superimposed on these background values. The main feature of the record is a >3‰ increase at 657 mbsf to −23·6‰, which is accompanied by increases in $\delta^{13}C$ of *n*-C27 and *n*-C25 *n*-alkanes (reflecting terrestrial leaf waxes), *n*-C19 *n*-alkanes (algal organic matter) and *n*-C31 ββ-hopanes (bacterial biomass) of a similar magnitude, albeit offset to slightly lighter values. The positive $\delta^{13}C$ excursion can be broken into two parts, with a lower interval (656·79 to 656·49 mbsf) of higher $\delta^{13}C_{TOC}$, and a second interval (656·49 to 655·68 mbsf) of slightly lower $\delta^{13}C_{TOC}$. The abundance of total organic carbon (%TOC) fluctuates around minimum values of *ca* 0·1 to 0·5% throughout the section, with common increases to *ca* 3 to 15% (Fig. 3). The first significant increase in %TOC (to *ca* 15%) occurs during the major positive C-isotope excursion that correlates with and can be used to define the duration of OAE-2 (Tsikos *et al.*, 2004; Jarvis *et al.*, 2011). However, at Site 1138, the timing of this increase stratigraphically lags the onset of the positive C-isotope excursion, thereby demonstrating a difference in the timing of carbon burial on the Kerguelen Plateau with respect to average global carbon burial in the latest Cenomanian.

The composition of the bulk organic matter is represented geochemically by the hydrogen index [HI = (S2/%TOC)*100, where S2 (mg g^{-1} TOC) is the hydrocarbon yield during Rock-Eval pyrolysis]. Values of HI reflect the presence of hydrogen-rich organic matter versus the presence of hydrogen-poor (higher plant) organic matter, although values can also be lowered by oxidative degradation and thermal maturity; HI fluctuates around a minimum of <50, with short-term excursions to maximum values of *ca* 100 to 300 upward from 657 mbsf. The transient increases in HI are tightly correlated with %TOC, demonstrating a close coupling between the amount and composition of buried organic matter (Fig. 3). Overall, Rock-Eval pyrolysis indicators (HI versus OI) tend to characterize the bulk of the organic matter as a mixture of type II algal and type IV hydrogen-poor (oxidized) algal matter (Fig. 4A). The weak positive

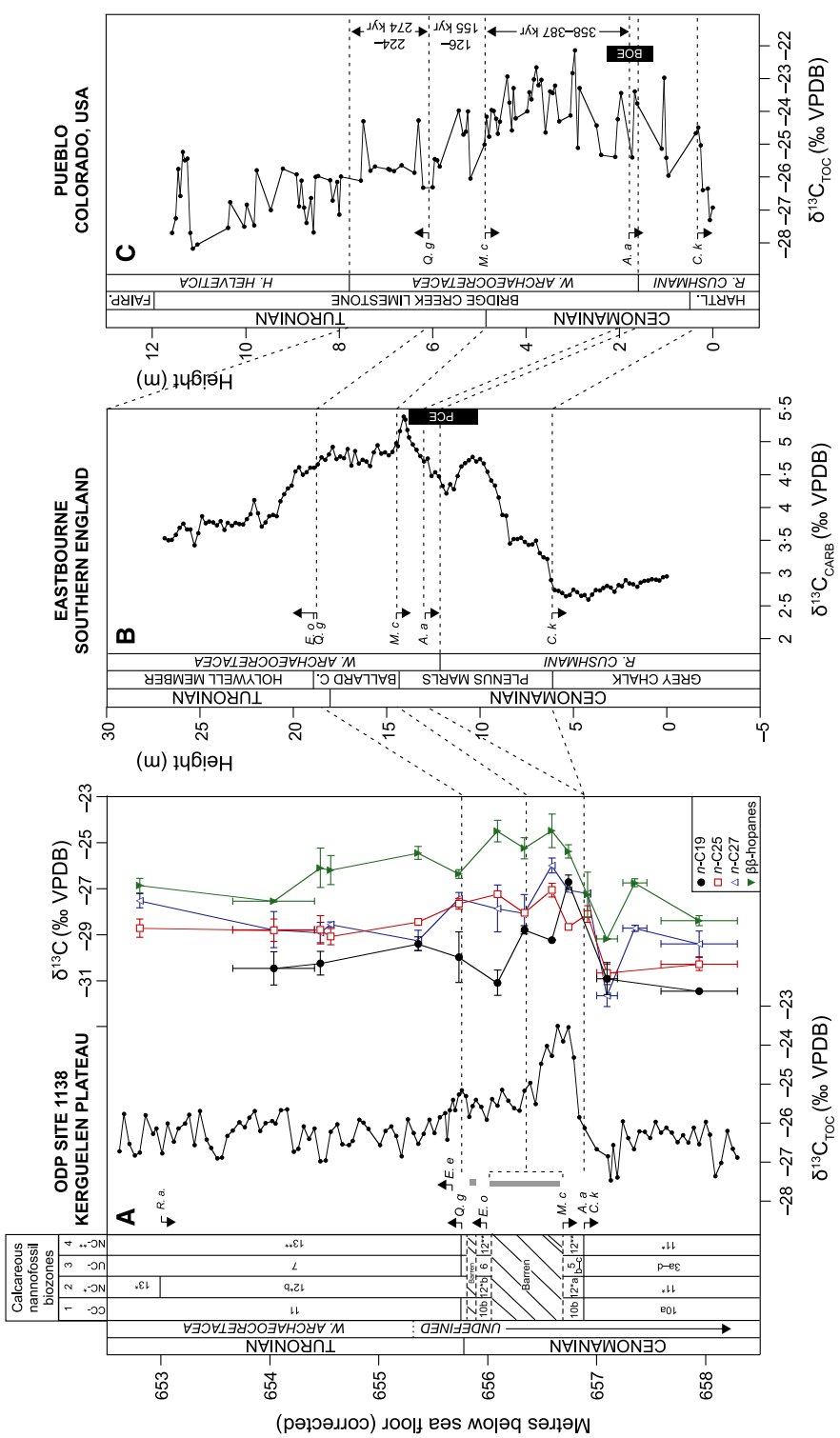

Fig. 2. Stratigraphic correlation of Site 1138 to chemostratigraphically and biostratigraphically constrained Cenomanian–Turonian boundary locations worldwide. (A) $\delta^{13}C_{TOC}$ and compound-specific $\delta^{13}C$ for Site 1138, plotted against foraminiferal biozones (Shipboard Scientific Party, 2000; Holbourn & Kuhnt, 2002), and nannofossil lowest and highest occurrences (this study). Vertical uncertainties on the compound-specific data indicate the depth ranges where samples had to be combined due to the low abundances of individual compounds. Horizontal uncertainties for the compound-specific data are the 1 SD of replicate analyses. (B) $\delta^{13}C_{CARB}$ data from the Eastbourne section, southern England (Tsikos *et al.*, 2004), plotted against foraminiferal biozones and nannofossil highest and lowest occurrences (Gale *et al.*, 1993; Paul *et al.* 1999). (C) $\delta^{13}C_{TOC}$ data from the Portland-1 core, Pueblo, USA (Sageman *et al.*, 2006), plotted against foraminiferal biozones and nannofossil highest and lowest occurrences (Pratt & Threlkeld, 1984; Bralower & Bergen, 1998; Keller & Pardo, 2004; Kennedy *et al.*, 2005). Dashed lines are correlations based on the chemostratigraphic and biostratigraphic datum levels, discussed in the text. The Cenomanian–Turonian boundary has been located based on the last relatively elevated C-isotope data point following the OAE-2 plateau intervals (Tsikos *et al.*, 2004). Nannofossil zones after: '1' Sissingh (1977); '2' Bralower *et al.* (1995); '3' Burnett (1998); '4' Tsikos *et al.* (2004). *C. k.* = *Corollithion kennedyi*; *A. a.* = *Axopodorhabdus albianus*; *M. c.* = *Microstaurus chiastius*; *E. o.* = *Eprolithus octopetalus*; *Q. g.* = *Quadrum gartneri*; *E. e.* = *Eprolithus eptapetalus*; *R. a.* = *Rhagodiscus asper*. The grey vertical line in panel (A) indicates an interval barren of nannofossils. PCE, Plenus Cold Event; BOE, Benthic Oxic Event.

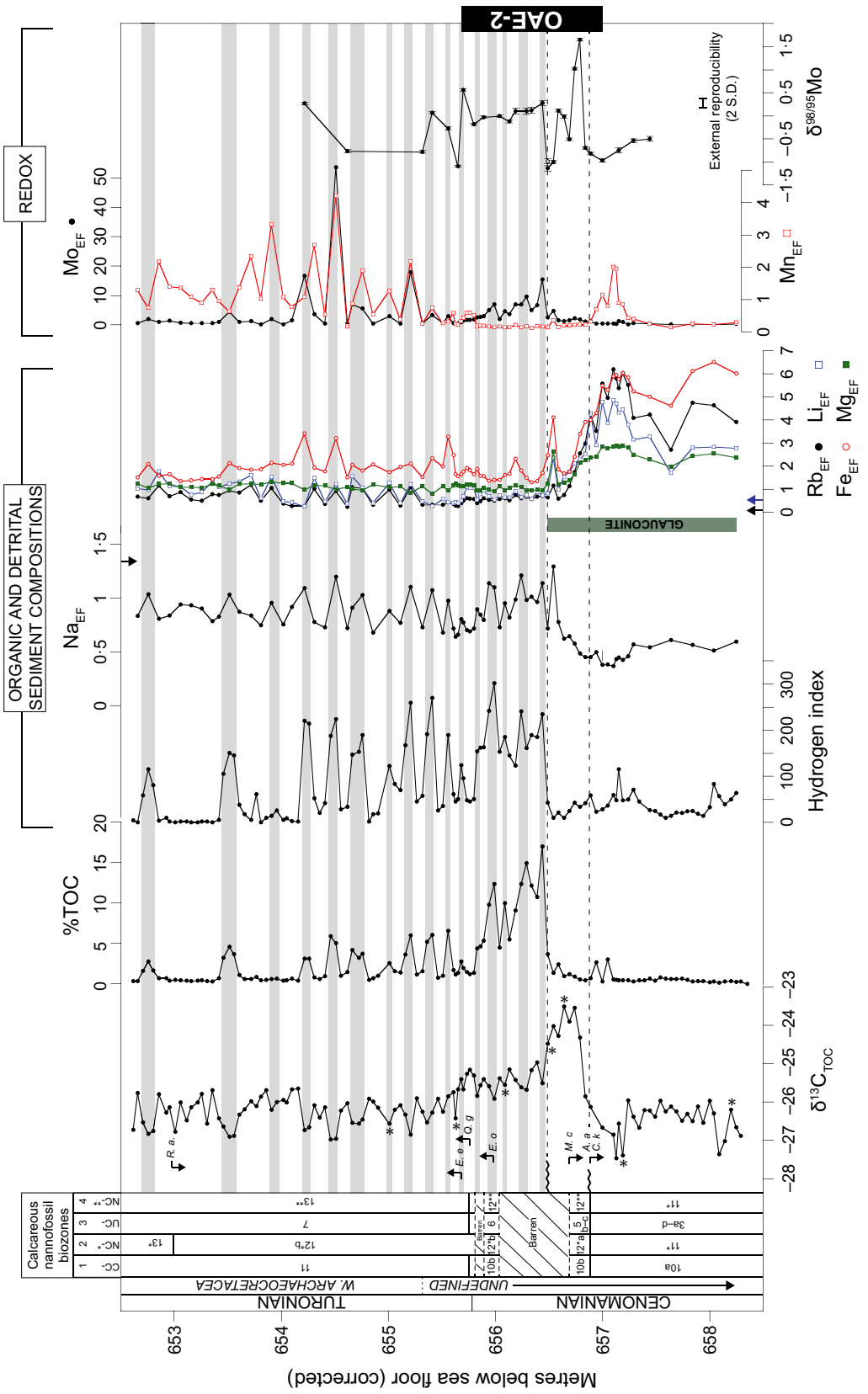

Fig. 3. Geochemical data for Site 1138 plotted against core depth corrected for post-recovery core expansion. Samples examined for organic macerals are indicated by an asterisk. Zigzag lines indicate stratigraphic hiatuses or intervals of slow sedimentation. Horizontal shaded bands indicate intervals of elevated organic-carbon concentration. The black and blue arrows indicate the enrichments of Rb and Li over average continental-crust concentrations in basalts drilled at Site 1138 (Neal *et al.*, 2002). The 2 SD external reproducibility for the $\delta^{98/95}$Mo data (±0·09‰) is shown as a horizontal error bar (see text for details). See Fig. 2 for details of nannofossil zonations.

Table 1. Calcareous nannofossil bioevents.

Calcareous nannofossil bioevents	Depth (mbsf)
HO *Rhagodiscus asper*	653·00
LO *Eprolithus eptapetalus*	655·70
LO *Quadrum gartneri*	655·75
LO *Eprolithus octopetalus*	655·99
HO *Microstaurus chiastius*	656·69
HO *Axopodorhabdus albianus*	656·89
HO *Corollithion kennedyi*	656·89
LO *Ahmuellerella octoradiata*	657·00

HO = Highest stratigraphic occurrence.
LO = Lowest stratigraphic occurrence.

correlation between %TOC and the *n*-C31 hopane ββ/(ββ+βα+αβ) ratio (Fig. 4B) is also suggestive of a contribution of older reworked organic matter (relatively fewer ββ hopanes) to TOC in the organic-lean intervals.

Organic petrography

Petrographic examination of the organic and inorganic components and mineral groundmass in six samples (Table 2) supports the inferences from organic geochemistry by showing the presence of macerals of the liptinite group as varying proportions of primary macerals such as liptodetrinite, *Bottryococcus* algae, acritarch and dinoflagellate remains, and secondary solid or migrabitumen, with higher proportions of these macerals occurring in the samples with higher %TOC and HI (Fig. 5; Table 2). There are very low amounts of vitrinite (terrestrial macerals) in all of the studied samples, with detectable amounts (*ca* 0·1 vol.%) occurring in only two samples stratigraphically above 657 mbsf. The low proportion of terrestrially derived organic matter throughout the section agrees well with the interpretation of low-HI samples from Rock-Eval pyrolysis as reflecting oxidized type IV algal matter. Furthermore, inertinite is present in low proportions in all studied samples above 656·49 mbsf, supporting the inference of oxidized type IV organic matter obtained from Rock-Eval pyrolysis.

Inorganic geochemistry

Enrichment factors for rubidium (Rb_{EF}), lithium (Li_{EF}) and iron (Fe_{EF}) range between *ca* 0·5 and *ca* 6·5, and have very similar stratigraphic fluctuations (Fig. 3). Enrichment factors are moderately high stratigraphically below 657·14 mbsf (Rb_{EF} = 6·2; Li_{EF} = 4·8; Fe_{EF} = 6·2). Above this level, enrichment factors of all three elements decrease to much lower values [(Rb_{EF} = 0·5 to 1·5; Li_{EF} = 0·5 to 1·5; Fe_{EF} = 1·4 to 3·4). Enrichment factors for sodium (Na_{EF}) show the opposite trend to Rb_{EF}, Li_{EF} and Fe_{EF}, with a

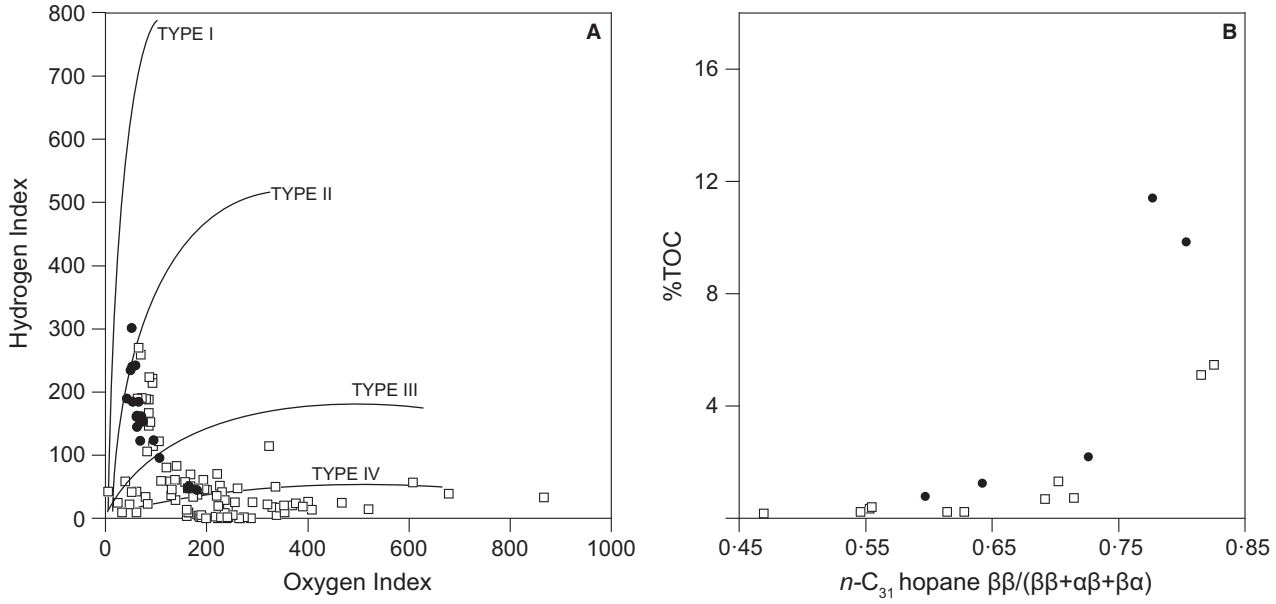

Fig. 4. Organic geochemical data for Site 1138. Filled circles are samples from within the OAE-2 interval of Site 1138. Open squares are all other data. (A) Characterization of bulk organic matter using Hydrogen Index versus Oxygen Index. (B) Thermal maturity of organic matter at Site 1138 using TOC versus the *n*-C31 hopane ββ/(ββ+βα+αβ) index. The data indicate a trend of decreasing thermal maturity at higher %TOC.

Table 2. Results of organic petrographic analyses

Depth	Vitrinite (%)		Liptinite (%)				Inertinite (%)		Minerals (%)														
			Telalginite		Lamal.					Ground-mass		Carbonates		Peloids						Pyrite			
	Auto.	Allo.	Acrit.	Dino.	Sh.	Lipt.	S. Bit.	Inertd.	Micr.	F. relics	Calc.	Clay	Is. Cr.	Cocc.	White	Orange	Glauc.	Mica	D. qrz	M. oxides	Crys.	Fram.	Epig.
655·01	–	–	1·0	–	–	3·4	1·7	0·1	0·6	4·9	76·2	10	–	0·2	0·1	–	–	–	–	–	0·8	0·5	0·5
655·63	0·1	–	0·7	0·1	0·1	3·0	1·2	0·1	0·3	1·0	81·2	6·9	0·4	0·6	0·6	–	0·4	–	0·1	1·1	0·6	0·7	0·9
656·08	–	–	1·3	0·2	–	3·6	5·5	0·3	9·5	2·3	51·2	18·2	1·4	–	0·7	–	0·5	–	0·4	0·3	2·8	1·7	0·1
656·49	0·1	–	0·4	0·2	–	0·6	3·0	0·1	1·0	1·0	78·3	9·7	0·7	1·0	1·1	0·9	–	–	0·1	1·1	0·6	0	0·1
656·64	–	–	0·2	0·1	–	0·2	0·5	–	0·3	4·5	59·7	23·4	0·1	–	0·4	–	7·8	0·1	0·4	1·7	0·6	0·1	–
657·19	–	–	0·1	–	–	0·1	–	–	–	1·4	24·1	5·9	–	–	–	–	67·8	–	–	0·1	0·4	0·1	–
658·20	–	–	0·4	–	–	0·2	0·3	–	–	3·1	38·6	0·3	–	–	–	–	56·6	–	0·2	0·2	0·1	–	–

Auto. – autochthonous; Allo. – allochthonous; Acrit. – acritarch; Dino. – dinoflagellates; Lamal. – lamalginite; Sh. – short; Lipt. – liptodetrinite; S. bit. – solid bitumen; Inertd. – inertodetrinite; Micr. – micrinite; F.relics – faunal relics; Calc. – calcareous; Is.cr. – isolated crystals; Cocc. – coccoliths; Glauc. – glauconite; D.qrt. – detrital quartz; M. oxides – metal oxides; Crys. – crystal; Fram. – framboidal pyrite; Epig. – epigenetic pyrite.

stepwise increase to *ca* 1·2 at 656·44 mbsf. Further up-section, Na_{EF} remains high and fluctuates between *ca* 0·7 and 1·2. The stepwise shifts in elemental abundances are accompanied by changes in the mineral composition of the deposits. The two lowermost samples examined contained 56·6 to 67·8 vol.% of glauconite. However, at 656·64 mbsf, glauconite is far less abundant (7·8 vol.%), and is only a negligible constituent of the samples examined from further up-section (<0·5 vol.%). These elemental and mineralogical associations indicate a decrease in the proportion of highly weathered clays versus less weathered primary minerals over the onset of the positive C-isotope excursion recorded at Site 1138.

Enrichment factors of the redox-sensitive elements molybdenum (Mo_{EF}) and manganese (Mn_{EF}) are both <0·5 below 656·49 mbsf, apart from a brief increase in Mn_{EF} to *ca* 2 between 657·15 and 656·94 mbsf. Above 656·44 mbsf, Mo_{EF} repeatedly increases over short intervals to *ca* 1·5 to 5·0 and Mn_{EF} repeatedly increases to higher values of *ca* 1 to 4 above 655·76 mbsf. Many of the elemental enrichment factors (Rb_{EF}, Li_{EF}, Fe_{EF}, Na_{EF}, Mn_{EF} and Mo_{EF}) fluctuate in tandem above 656·44 mbsf, suggesting a link between the processes governing sea-floor redox and sediment delivery.

Values of $\delta^{98/95}$Mo at the base of the studied section are −0·5 to −0·6‰, and increase above 657 mbsf to between −0·18‰ and 0·57‰. Above 655·70 mbsf, $\delta^{98/95}$Mo decreases towards lower values of −0·77‰ in the uppermost measured samples. This general positive excursion in $\delta^{98/95}$Mo is interrupted by two features: firstly, $\delta^{98/95}$Mo decreases to lower values of *ca* −1·10‰ in two short intervals at 656·49 mbsf and 655·55 mbsf; and, secondly, $\delta^{98/95}$Mo increases to 1·65‰ over a *ca* 5 cm interval beginning at 656·79 mbsf.

DISCUSSION

Stratigraphic succession and depositional environments of the Cenomanian–Turonian boundary interval at Site 1138

The stratigraphy of the deposits spanning the Cenomanian–Turonian boundary at Site 1138 can be described with new high-resolution $\delta^{13}C_{TOC}$, compound-specific $\delta^{13}C$ and nannofossil datasets, in combination with the published foraminiferal biostratigraphy for the core

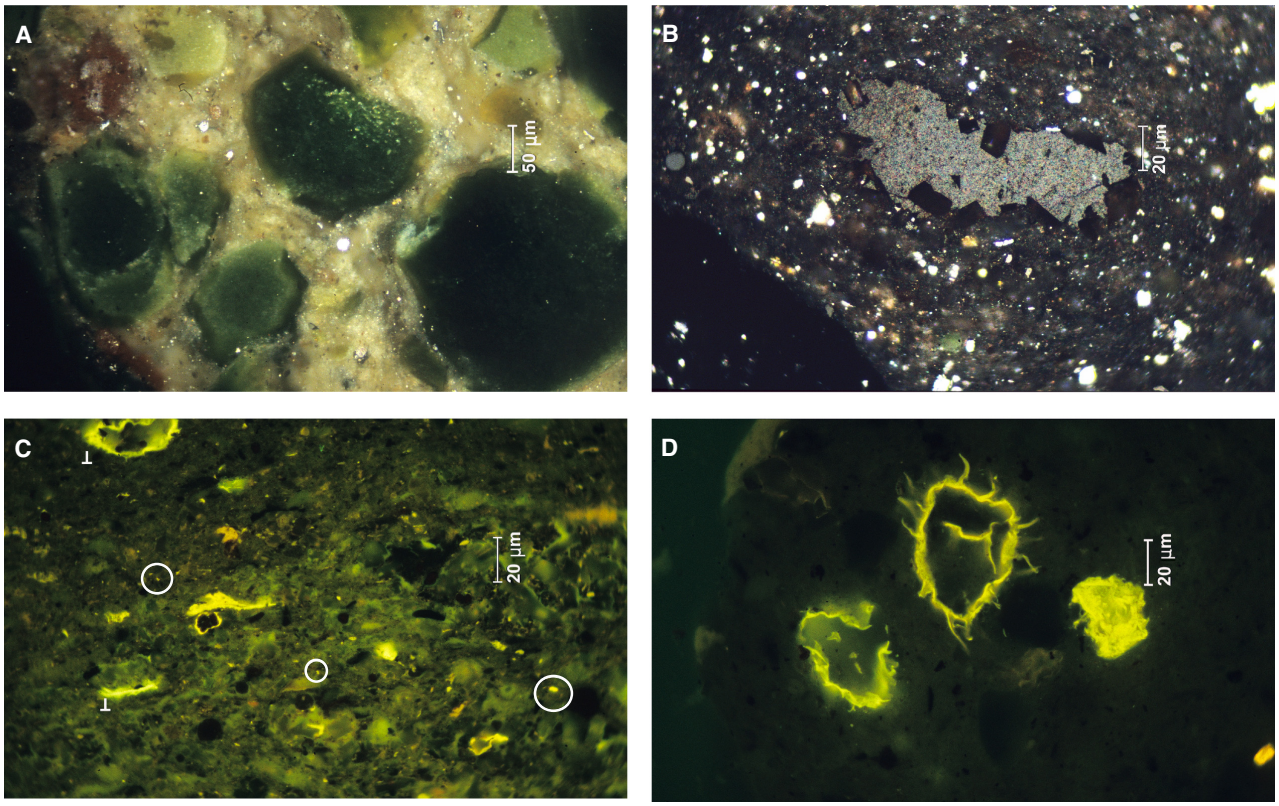

Fig. 5. Organic petrography of Site 1138 samples. (A) Photomicrograph of glauconite grains, showing a green colour in reflected white light, oil immersion. (B) Low reflecting heterogeneous migrabitumen in a large pore between carbonate crystals. Reflected white light, oil immersion. (C) Photomicrograph illustrating examples of liptodetrinite (enclosed in white circles) and telalginite (T). Fluorescence mode, oil immersion. (D) Photomicrograph of dinoflagellate cysts showing a green-yellow colour of high intensity. Fluorescence mode, oil immersion.

(Holbourn & Kuhnt, 2002). The similarity of the different C-isotope records, potentially recording marine and atmospheric carbon reservoirs, shows that the major positive C-isotope excursion at Site 1138 mainly records changes in global, rather than local, carbon cycling and, in conjunction with the nannofossil data, can be reliably correlated with the OAE-2 global C-isotope excursion (Tsikos *et al.*, 2004). These data are compared to the Cenomanian–Turonian record from the USGS Portland-1 research core (Pratt & Threlkeld, 1984; Keller & Pardo, 2004; Kennedy *et al.*, 2005; Sageman *et al.*, 2006), which is similar to the C/T GSSP (Cenomanian/Turonian Global Stratotype Section and Point) at Pueblo, Colorado; and Eastbourne, UK (Gale *et al.*, 1993; Tsikos *et al.*, 2004; Paul *et al.*, 1999; Jarvis *et al.*, 2006) in order to identify the completeness of the Site 1138 succession (Fig. 2).

The correlation in Fig. 2 indicates that the onset of OAE-2 is not captured within the ODP Site 1138 sedimentary succession. Three considerations support this argument. Firstly, the new high-resolution nannofossil biostratigraphy constrains the HO of *A. albianus* and *C. kennedyi* to the same stratigraphic level at Site 1138, prior to the increase in $\delta^{13}C_{TOC}$. At Pueblo and Eastbourne, the HO of *C. kennedyi* occurs in the upper *Rotalipora cushmani* zone, with the HO of *A. albianus* occurring higher upsection, during the *Whiteinella archaeocretacea* zone and within the interval recording the Plenus Cold Event/Benthic Oxic Event (Gale *et al.*, 1993; Bralower & Bergen, 1998; Paul *et al.*, 1999; Kennedy *et al.*, 2005). Thus, part of Zone CC10a (Sissingh, 1977), the upper part of Zone NC11* (of Bralower *et al.*, 1995 and Tsikos *et al.*, 2004) and Zones UC3e to UC5a (of Burnett, 1998) are not present in the core.

The second line of evidence for a hiatus near the base of the studied succession is that the bulk and compound-specific C-isotope data contain only one positive shift, while most OAE-2 C-isotope records contain two positive shifts near the onset of the event, separated by a brief return to slightly less positive values (e.g. Pratt &

Threlkeld, 1984; Tsikos *et al.*, 2004). The compound-specific C-isotope data suggest that changes in organic-matter composition do not drive the shift in $\delta^{13}C_{TOC}$, or hide the presence of a second positive excursion, and thus that one such shift is missing. The inferred chemostratigraphic hiatus agrees with the nannofossil zonation in showing that the early stages of OAE-2 are not recorded at Site 1138. Consequently, the Plenus Cold Event, which falls stratigraphically within this missing interval, cannot be traced into the Southern Hemisphere using the Site 1138 deposits.

Thirdly, the presence of a hiatus at the base of the positive C-isotope excursion is also supported by the high abundance of glauconite grains below *ca* 656·79 mbsf, reflected in enrichments of Fe and Mg (Figs 3 and 5A). Glauconite typically requires very slow sedimentation rates and mildly reducing conditions in sediment micro-pores to precipitate, a process that is typically accompanied by dissolution and alteration of the host substrate (Odin & Matter, 1981; Chafetz & Reid, 2000). Corresponding high enrichments of Rb and Li can be explained by the partitioning of these elements into secondary minerals during the chemical weathering of primary rocks (Pistiner & Henderson, 2003; Pogge van Strandmann *et al.*, 2006). The presence of glauconite points to a shallow-marine environment with either *in situ* alteration of primary minerals to clays, or the delivery of highly weathered clays from nearby exposed portions of the central Kerguelen Plateau, and supports the inference of a break in sedimentation, or an extremely slow sedimentation rate.

The enrichments of Fe, Mg, Rb and Li decline abruptly above the onset level of the CIE, at *ca* 657 mbsf, and point to a reduction of *in situ* glauconite and clay-mineral formation (or the delivery of clays from subaerial landmasses). These changes can be explained by an increase in relative sea-level (RSL) that would have created accommodation space for more rapid sedimentation on the Kerguelen Plateau margin. A transgressive trend has been identified at many OAE-2 successions worldwide, an observation that has been used to propose a eustatic sea-level rise on the order of a few tens of metres in the latest Cenomanian (e.g. Arthur *et al.*, 1987; Gale *et al.*, 2008). It is not likely that plateau subsidence occurring during the hiatus in sedimentation at the base of OAE-2 alone could have caused the RSL rise, given that the duration of the hiatus is not likely to exceed *ca* 400 kyr, and is probably closer to *ca* 200 kyr (Sageman *et al.*, 2006; Voigt *et al.*, 2008; Meyers *et al.*, 2012; Eldrett *et al.*, 2015). Assuming a 22 mm kyr^{-1} subsidence rate, these durations would allow only a modest *ca* 4 to 9 m of RSL rise. These subsidence estimates may be further reduced when it is considered that enrichments of Mn and Fe, and a decrease in $\delta^{98/95}$Mo at 656·54 mbsf, indicate the re-oxidation of sediment pore waters and perhaps the presence of a second sedimentary hiatus. A eustatic contribution to RSL rise is needed to accommodate the significant shift in sedimentary facies, along with the accompanying changes in sediment geochemistry. Such a rise is not inconceivable in light of the evidence for sea-level rise at numerous locations during the late Cretaceous (Hancock & Kauffman, 1979).

The delayed onset of maximum organic-matter burial during OAE-2 at Site 1138 compared with other locations worldwide, therefore, can be explained partly by the effect of local RSL rise. Relative sea-level rise would have created accommodation space for organic-carbon burial around the margins of the central Kerguelen Plateau during OAE-2, but not until several tens of thousands of years after the start of the CIE. Enrichments in %TOC similar to those observed at Site 1138 have also been identified at ODP Site 763 on Exmouth Plateau, off Western Australia (Thurow *et al.*, 1992), and have been linked to the presence of an oxygen minimum zone impinging on the upper continental slope. It is interesting to speculate whether or not the enhanced organic-matter burial at the relatively shallow palaeodepths of Sites 1138 and 763 was influenced by a common oxygen-depleted water-mass extending over much of the proto-Indian Ocean.

Controls on cyclic organic-matter burial on the central Kerguelen Plateau

The Cenomanian–Turonian record of organic-carbon enrichment at Site 1138 is highly cyclic up-section from the level of initial increase in %TOC that characterizes the OAE-2 interval (Fig. 3). The low abundance of vitrinite in the studied samples indicates that the cyclicity in TOC is not likely to be explained by large changes in the flux of terrestrial organic matter. Likewise, low T_{max} values and *n*-C31 hopane ββ/(ββ+βα+αβ) ratios >*ca* 0·5 are not consistent with large changes in organic-matter maturity across each TOC cycle, although slightly lower *n*-C31 hopane ββ/(ββ+βα+αβ) ratios during

%TOC minima in the lower Turonian might point to localized re-working of older organic matter from the Kerguelen Plateau at these times (Fig. 4). These observations therefore require a greater burial efficiency of marine-derived organic matter during TOC-rich intervals, which may have been promoted either by a reduction in seawater oxygen concentrations that inhibited organic-matter remineralization (preservation), and/or by a higher flux of organic matter to the sea floor (higher productivity).

Peaks in the %TOC and HI cycles correlate with higher abundances of molybdenum and uranium, which become enriched in sediments under low-oxygen conditions, and with low abundances of manganese, which becomes mobile under lowered oxygen conditions (Crusius *et al.*, 1996; Tribovillard *et al.*, 2006). These elemental associations support the notion of a redox influence on the TOC cyclicity at Site 1138, which might have been caused by expansions and contractions of an oxygen minimum zone impinging on the margin of the central Kerguelen Plateau. Such fluctuations in the depth of the oxygen minimum zone must have been driven either by changes in oxygen consumption related to local organic-carbon remineralization, or alternatively to changes in the production of oxygen-depleted deepwater masses further afield. In support of the latter mechanism, Earth-system model results have indicated that large areas of the deep proto-Indian Ocean sea floor in the vicinity of the central Kerguelen Plateau might have experienced anoxia during OAE-2, with surrounding shallow sea-floor regions remaining oxic (Monteiro *et al.*, 2012). Repeated shoaling and deepening of an oxygen-depleted water mass might possibly have controlled the rate of carbon oxidation in shallow pore waters at Site 1138, and thus promoted the observed cyclicity in organic-carbon burial.

However, because variations in sea-floor redox conditions can also be controlled by changes in the flux of organic matter to the sea floor, productivity changes might also have played a major role in driving the %TOC cycles at Site 1138. Such a relationship has been documented for the proto-North Atlantic Ocean (Kuypers *et al.*, 2004), where productivity, redox and %TOC might all ultimately be linked by periodic variations in the flux of weathered nutrients from surrounding landmasses, as well as changes in the basin redox (Poulton *et al.*, 2015; Dickson *et al.*, 2016). At Site 1138, indications of changes in primary productivity during each %TOC cycle derive from two lines of evidence. Firstly, low nitrogen-isotope compositions of the bulk organic matter during the OAE-2 interval (Meyers *et al.*, 2009) suggest a greater abundance of nitrogen-fixing bacteria living in poorly ventilated surface waters, although the data may also be consistent with high rates of production by eukaryotes, coupled with recycling of NH_4 to surface waters (Higgins *et al.*, 2012). Changes in the community structure of primary producers might also have been encouraged by inhibition of enzyme function in marine algae due to the low abundances of bio-essential trace metals (Zn and Mo) in seawater (Hetzel *et al.*, 2009). Secondly, the association of peaks in the TOC and HI cycles with higher Na enrichment factors (Fig. 3) circumstantially points to higher primary productivity at these times. Sodium is highly depleted in weathered rocks, due to its removal during feldspar alteration (Nesbitt & Young, 1982), and intervals of relative enrichment in Site 1138 therefore record the delivery of less highly weathered detrital sediments, presumably due to incongruent weathering of exposed basalts on the central Kerguelen Plateau.

Taken together, these arguments suggest that the local seawater nutrient inventory, controlled by periodic variations in weathering rates on the central Kerguelen Plateau, acted as a primary control on cyclic organic-matter burial at Site 1138. The remineralization of the (periodically) enhanced organic-matter fluxes probably lowered seawater oxygen concentrations sufficiently for redox to further raise the efficiency of organic-matter burial.

The periodic nature of organic-carbon burial on the central Kerguelen Plateau during the early Turonian suggests a climatic control, potentially related to changes in temperature and/or precipitation regimes. The duration between the LO of *Q. gartneri* and LO of *Helvetoglobotruncata helvetica* has been estimated as *ca* 225 ka from cyclostratigraphic tuning of the USGS Portland Core-1 at Pueblo, Colorado (Sageman *et al.*, 2006) and *ca* 690 ± 130 ka from the Shell Iona-1 research core at Del Rio, Texas (Eldrett *et al.*, 2015). Transferring these durations to the 3·94 to 4·44 m equivalent section at Site 1138, estimated from the new nannofossil data presented here, and the existing foraminiferal biostratigraphy of Holbourn & Kuhnt (2002), generates sedimentation rate estimates of 0·57 to 1·97 cm ka^{-1}. Sedimentation

rates in this range imply average durations of *ca* 20 to 70 ka for the 10/11 cycles in %TOC spanning the LO of *Q. gartneri* to the top of the studied section at Site 1138. These durations span the range of orbital precession (*ca* 23 kyr) and orbital obliquity (*ca* 41 kyr) and might implicate monsoonal dynamics and/or changes in ocean circulation as possible climatic drivers for the observed coupling between weathering and organic-matter burial on the central Kerguelen Plateau.

Seawater trace-metal inventories

Two geochemical indices (Mo_{EF}/U_{EF} and Mo/TOC) have been used as palaeoenvironmental indicators for marginal ocean basins (Algeo & Tribovillard, 2009; Tribovillard *et al.*, 2011; Algeo & Lyons, 2006; Algeo & Rowe, 2011). The Mo_{EF}/U_{EF} proxy exploits the differing sensitivity of these two elements to euxinic and anoxic depositional conditions, respectively, in order to characterize local redox changes, and the degree of local watermass restriction. In open-marine settings, Mo-U co-variation in sediments proceeds along a trajectory that initially enriches U under sub-oxic conditions [at the Fe(III)–Fe(II) boundary] before the development of anoxic and euxinic conditions starts to enrich Mo. Deviations from this trajectory indicate preferential enrichment of Mo due to a strong hydrographic connection with the global ocean, coupled with a strong chemocline and the presence of Fe-Mn 'shuttling' across this boundary (Algeo & Tribovillard, 2009; Tribovillard *et al.*, 2011). The sedimentary Mo/TOC proxy utilizes the common enrichment of both of these parameters in the oxygen-depleted environments commonly found within hydrographically restricted marginal marine basins (Algeo & Lyons, 2006). As the trace-metal inventory within the basin changes, due to drawdown under low-oxygen conditions coupled with limited re-supply by inter-basinal transfer of water masses, the sedimentary Mo/TOC ratio decreases. Different Mo/TOC gradients have been observed for modern marine basins characterized by different seawater residence times. The Mo/TOC proxy can consequently be used as an indicator of Mo concentrations in basinal seawater (Algeo & Lyons, 2006; Algeo & Rowe, 2011).

For Site 1138, the Mo_{EF}/U_{EF} data follow the present-day open-marine trajectory, with an initial enrichment of U under sub-oxic conditions, followed by progressive enrichment of Mo as anoxic conditions developed (Fig. 6A). However, despite the relative enrichments of U and Mo

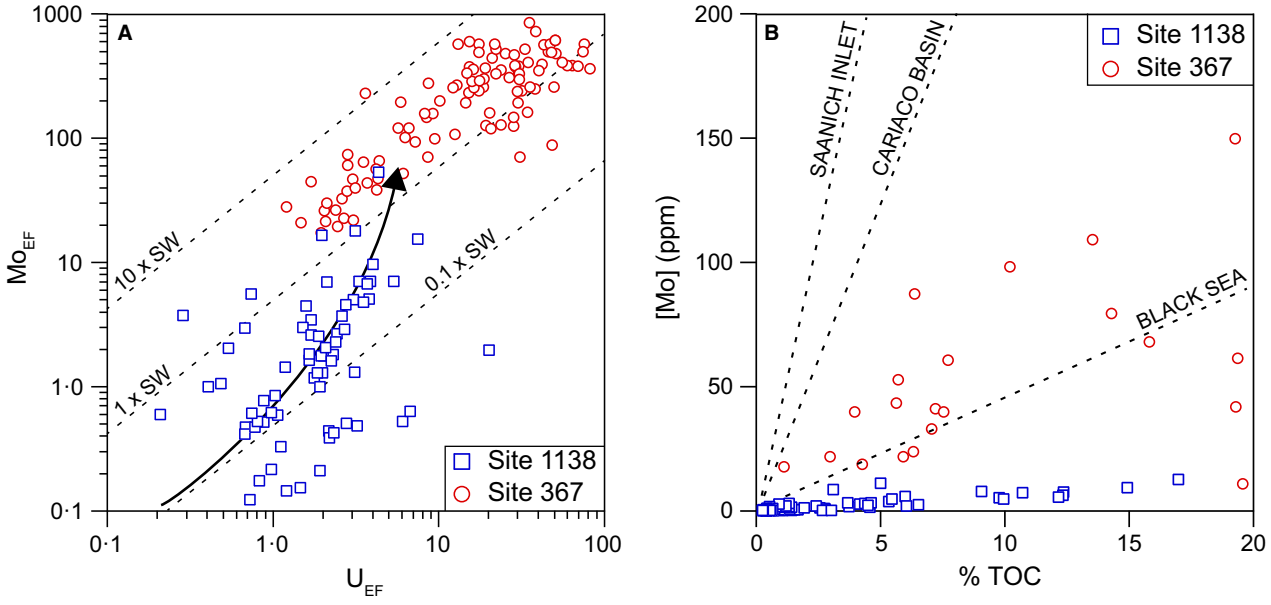

Fig. 6. Elemental co-variations. (A) Mo_{EF} versus U_{EF} for Site 1138 (open blue squares) and Site 367 (open red circles). Dashed lines show the sedimentary enrichments corresponding to modern seawater Mo/U molar ratios of *ca* 7·5 to 7·9 (Algeo & Tribovillard, 2009). Arrow indicates an open-marine trajectory of U enrichment followed by Mo enrichment under increasingly sulphidic depositional conditions (Algeo & Tribovillard, 2009). (B) Mo versus %TOC for Site 1138 (open blue squares) and Site 367 (open red circles). Dashed lines show the Mo/TOC gradients for modern marine basins experiencing differing degrees of watermass restriction (Algeo & Lyons, 2006).

during OAE-2, two lines of evidence show that euxinic conditions did not develop on the central Kerguelen Plateau: (i) Mo_{EF}/U_{EF} values never increase above the seawater molar ratio of *ca* 7·7, the level that would suggest the presence of sulphidic depositional conditions; and (ii) $\delta^{98/95}Mo$ values during the OAE-2 interval of Site 1138 are <0·5‰ (Fig. 3), which is significantly lower than temporally coeval data from the highly euxinic proto-North Atlantic Ocean (Westermann *et al.*, 2014; Dickson *et al.*, 2016) indicating the presence of sulphidic pore waters, but not a sulphidic water column. In contrast, the Mo/TOC data (Fig. 6B) follow a gradient that is significantly lower than the present-day Black Sea, which is characterized by highly restricted deep watermasses, with Mo concentrations >90% lower than in the present-day open ocean (Pilipchuk & Volkov, 1974; Emerson & Huested, 1991; Nägler *et al.*, 2011). The very low abundance of terrestrial macerals (Table 2) rules out significant changes in organic-matter type as a primary control on the Mo/TOC ratios; likewise, the relative enrichments in trace metals and Mo-isotope compositions across the Site 1138 black-shale interval confirm that localized oxygenation [as seen in the Western Interior Seaway (Eldrett *et al.*, 2014)] is not responsible. Therefore, reconciling a low Mo/TOC gradient with a hydrographically unrestricted setting requires an extremely low concentration of Mo in global ocean seawater, rather than a locally restricted hydrographic regime.

These observations are the first of their kind from outside of the proto-North Atlantic Ocean to demonstrate the widespread and global nature of trace-metal depletion during OAE-2. However, widespread trace-metal drawdown does not necessarily point towards a 'globally' euxinic ocean, but rather a significant spread of deoxygenated zones occupying <10% of the global sea floor that acted as large 'sinks' for redox-sensitive metals (Montoyo-Pina *et al.*, 2010; Owens *et al.*, 2013; Westermann *et al.*, 2014). The observation of an extremely low Mo inventory in global seawater during OAE-2 also highlights the pitfalls of using Mo/TOC gradients as quantitative indicators of basin palaeohydrology. Van Helmond *et al.* (2014) recently used a Mo/TOC gradient from DSDP Site 367 in the central proto-North Atlantic Ocean to infer a watermass residence time of 500 to 4000 years during OAE-2, by comparison to the present-day Black Sea Mo/TOC gradient. However, this estimate is probably inaccurate for two reasons. Firstly, the global Mo inventory was considerably depleted compared with the present day, thus lowering 'apparent' Mo/TOC ratios and inhibiting direct comparison with present-day analogues. Secondly, additional sedimentary Mo enrichment at Site 367 may have occurred due to Mo 'shuttling' across a sharply developed chemocline, by adsorption and desorption to Fe/Mn-oxyhydroxides. Figure 6B demonstrates that the Mo/TOC gradient was actually lower at the hydrographically exposed central Kerguelen Plateau than in the restricted proto-North Atlantic Ocean. Although elemental proxies are clearly very valuable palaeoceanographic tools, caution is required when trying to draw quantitative inferences from these data.

CONCLUSIONS

New palaeontological and geochemical data from Ocean Drilling Program (ODP) Site 1138 on the central Kerguelen Plateau allow a detailed view of the environmental changes that affected the mid-latitude Southern Hemisphere across the Cenomanian–Turonian boundary interval. The initial onset and early stages of Oceanic Anoxic Event 2 (OAE-2) on the central Kerguelen Plateau had a very close temporal relationship with an episode of relative sea-level rise that brought to an end a period of glauconite formation in poorly oxygenated, slowly accumulating shallow-marine sediments, that prevented the early stages of OAE-2 from being recorded in the sedimentary succession of Site 1138 (Fig. 7A). An increase in water depth is credited with creating the accommodation space to allow the accumulation and burial of deeper marine chalks and marls during the OAE-2 interval and the early Turonian (Fig. 7B and C), and explaining the apparent lag in maximum organic-matter burial during OAE-2 at Site 1138 compared with other locations worldwide. Cyclic episodes of organic-matter burial during OAE-2 and during the early Turonian appear to have been productivity-driven phenomena, related to variations in the delivery of nutrients by the weathering of exposed portions of the central Kerguelen Plateau. In turn, trace-element concentration data show that enhanced carbon burial was aided by reductions in bottom-water oxygen concentrations, although Mo-isotope and elemental ratios indicate that this location was not affected by pervasive sulphidic depositional conditions. Sediments deposited under locally oxygen-depleted conditions at Site 1138, with minimal change in organic-matter type, provide the first

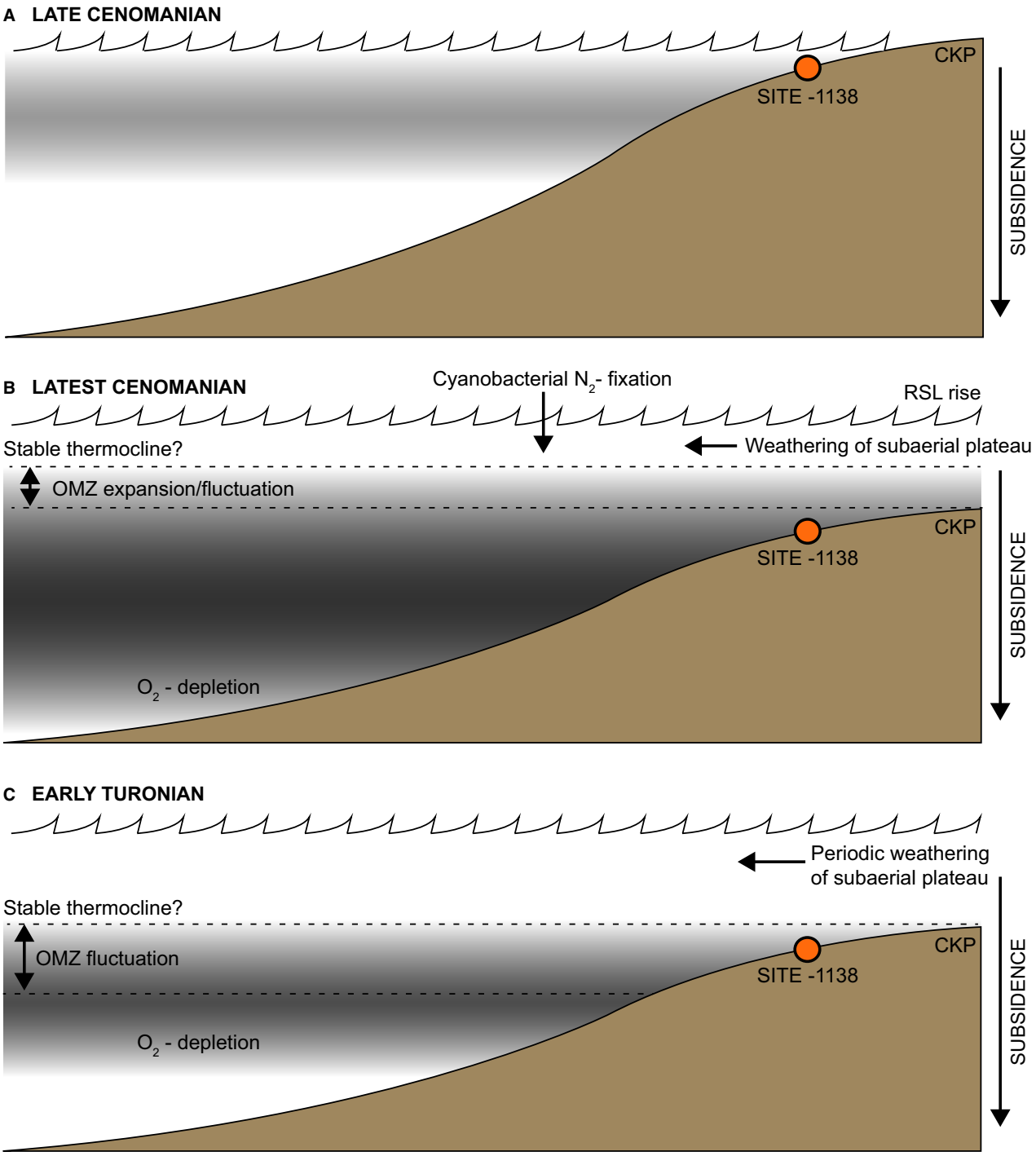

Fig. 7. Palaeoceanographic model for organic-carbon burial on the central Kerguelen Plateau from the late Cenomanian to early Turonian. Model constructed from data presented in this paper, as well as from Holbourn & Kuhnt (2002) and Meyers *et al.* (2009). Details are discussed in the text. CKP, Central Kerguelen Plateau; RSL, relative sea-level; OMZ, oxygen minimum zone.

clear evidence from outside the proto-North Atlantic Ocean that there was a dramatic global drawdown in the oceanic trace-metal inventory during OAE-2.

ACKNOWLEDGEMENTS

We thank Steve Wyatt, Peter Ditchfield, Phil Holdship and Alan Hsieh for laboratory support

and Shell Global Solutions International BV for funding. The manuscript was improved by the comments of an anonymous reviewer and the Associate Editor, Ulrich Heimhofer. Samples from ODP Site 1138 were provided by the International Ocean Discovery Programme. Raw data are available from the authors on request. The authors have no conflict of interests to declare.

REFERENCES

Adams, D.D., **Hurtgen, M.T.** and **Sageman, B.B.** (2010) Volcanic triggering of a biogeochemical cascade during Oceanic Anoxic Event 2. *Nat. Geosci.*, **3**, 201–204.

Algeo, T.J. and **Lyons, T.W.** (2006) Mo-total organic-carbon covariation in modern anoxic marine environments: implications for analysis of paleoredox and paleohydrologic conditions. *Paleoceanography*, **21**, PA1016. doi:10.1029/2004PA001112.

Algeo, T.J. and **Rowe, H.** (2011) Paleoceanographic applications of trace-metal concentration data. *Chem. Geol.*, **324–325**, 6–18.

Algeo, T.J. and **Tribovillard, N.** (2009) Environmental analysis of paleoceanographic systems based on molybdenum-uranium covariation. *Chem. Geol.*, **268**, 211–225.

Arthur, M.A., **Schlanger, S.O.** and **Jenkyns, H.C.** (1987) The Cenomanian–Turonian Oceanic Anoxic Event II: Palaeoceanographic controls on organic-matter production and preservation. In: *Marine Petroleum Source Rocks* (Eds J. Brooks and A.J. Fleet), *J. Geol. Soc. London Spec. Publ.*, **26**, 401–420.

Behar, F., **Beaumont, V.** and **De Penteado, H.L.** (2001) Rock-Eval 6 technology: performances and development. *Oil Gas Sci. Technol.*, **56**, 111–134.

Blättler, C.L., **Jenkyns, H.C.**, **Reynard, L.M.** and **Henderson, G.M.** (2011) Significant increases in global weathering during Oceanic Anoxic Events 1a and 2 indicated by calcium isotopes. *Earth Planet. Sci. Lett.*, **309**, 77–88.

Bralower, T.J. and **Bergen, J.A.** (1998) Cenomanian-Santonian calcareous nannofossil biostratigraphy: a transect of cores drilled across the Western Interior Seaway. In: *Stratigraphy and Paleoenvironments of the Cretaceous Western Interior Seaway, USA* (Eds W.E. Dean and M.A. Arthur), *SEPM Conc. Sedimentol. Paleontol.*, **6**, 59–77.

Bralower, T.J., **Leckie, R.M.**, **Sliter, W.V.** and **Thierstein, H.R.** (1995) An integrated Cretaceous timescale. In: *Geochronology Time Scales and Global Stratigraphic Correlation* (Eds W.A. Berggren, D.V. Kent, M.-P. Aubry and J. Hardenbol), *SEPM Spec. Publ.*, **54**, 65–79.

Burnett, J.A. (1998) Upper Cretaceous. In: *Calcareous Nannofossil Biostratigraphy* (Ed. P.R. Bown), pp. 132–199. Chapman and Hall, London.

Chafetz, H.S. and **Reid, A.** (2000) Syndepositional shallow-water precipitation of glauconite minerals. *Sed. Geol.*, **136**, 29–42.

Crusius, J., **Calvert, S.**, **Pedersen, T.** and **Sage, D.** (1996) Rhenium and molybdenum enrichments in sediments as indicators of oxic, suboxic and sulphidic conditions of deposition. *Earth Planet. Sci. Lett.*, **145**, 65–78.

Dickson, A.J., **Jenkyns, H.C.**, **Porcelli, D.**, **van den Boorn, S.** and **Idiz, E.** (2016) Basin-scale controls on the molybdenum-isotope composition of seawater during Oceanic Anoxic Event 2 (Late Cretaceous). *Geochim. Cosmochim. Acta*, **178**, 291–306.

Duncan, R.A. (2002) A time frame for construction of the Kerguelen Plateau and Broken Ridge. *J. Petrol.*, **43**, 1109–1119.

Du Vivier, A.D.C., **Selby, D.**, **Sageman, B.B.**, **Gröcke, D.R.** and **Voigt, S.** (2014) Marine $^{187}Os/^{188}Os$ isotope stratigraphy reveals the interaction of volcanism and ocean circulation during Oceanic Anoxic Event 2. *Earth Planet. Sci. Lett.*, **389**, 23–33.

Eldrett, J.S., **Ma, C.**, **Bergman, S.C.**, **Lutz, B.**, **Gregory, F.J.**, **Dodsworth, P.**, **Phipps, M.**, **Hardas, P.**, **Minisini, D.**, **Ozkan, A.**, **Ramezani, J.**, **Bowring, S.A.**, **Kamo, S.L.**, **Macaulay, C.** and **Kelly, A.** (2015) An astronomically calibrated stratigraphic of the Cenomanian, Turonian and earliest Coniacian from the Cretaceous Western Interior Seaway, USA: implications for global chronostratigraphy. *Cretaceous Res.*, **56**, 316–344.

Eldrett, J.S., **Minisini, D.** and **Bergman, S.C.** (2014) Decoupling of the carbon cycle during Oceanic Anoxic Event 2. *Geology*, **42**, 567–570.

Emerson, S.R. and **Huested, S.S.** (1991) Ocean anoxia and the concentrations of molybdenum and vanadium in seawater. *Mar. Chem.*, **34**, 177–196.

Frey, F.A., **Coffin, M.F.**, **Wallace, P.J.**, **Weis, D.**, **Zhao, X.**, **Wise, S.W., Jr**, **Wähnert, V.**, **Teagle, D.A.H.**, **Saccocia, P.J.**, **Reusch, D.N.**, **Pringle, M.S.**, **Nicolaysen, K.E.**, **Neal, C.R.**, **Mller, R.D.**, **Moore, C.L.**, **Mahoney, J.J.**, **Keszthelyi, L.**, **Inokuchi, H.**, **Duncan, R.A.**, **Delius, H.**, **Damuth, J.E.**, **Damasceno, D.**, **Coxall, H.K.**, **Borre, M.K.**, **Boehm, F.**, **Barling, J.**, **Arndt, N.T.** and **Antretter, M.** (2000) Origin and evolution of a submarine large igneous province: the Kerguelen Plateau and Broken Ridge, southern Indian Ocean. *Earth Planet. Sci. Lett.*, **176**, 73–89.

Frijia, G. and **Parente, M.** (2008) Strontium isotope stratigraphy in the upper Cenomanian shallow-water carbonates of the southern Apennines: short-term perturbations of marine $^{87}Sr/^{86}Sr$ during the oceanic anoxic event 2. *Palaeogeogr. Palaeoclimatol. Palaeoecol.*, **261**, 15–29.

Gambacorta, G., **Jenkyns, H.C.**, **Russo, F.**, **Tsikos, H.**, **Wilson, P.A.**, **Faucher, G.** and **Erba, E.** (2015) Carbon- and oxygen-isotope records of mid-Cretaceous Tethyan pelagic sequences from the Umbria–Marche and Belluno Basins (Italy). *Newsl. Stratigr.*, **48**, 299–323.

Gale, A.S., **Jenkyns, H.C.**, **Kennedy, W.J.** and **Corfield, R.M.** (1993) Chemostratigraphy versus biostratigraphy: data from around the Cenomanian-Turonian boundary. *J. Geol. Soc.*, **150**, 29–32.

Gale, A.S., **Voigt, S.**, **Sageman, B.B.** and **Kennedy, W.J.** (2008) Eustatic sea-level record for the Cenomanian (Late Cretaceous) – extension to the Western Interior Basin, USA. *Geology*, **36**, 859–862.

Gavrilov, Y.O., **Shcherbinina, E.A.**, **Golovanova, O.V.** and **Pokrovskii, B.G.** (2013) The Late Cenomanian Paleoecological event (OAE 2) in the Eastern Caucasus Basin of Northern Peri-Tethys. *Lithol. Mineral Resour.*, **48**, 457–488.

Hancock, J.M. and **Kauffman, E.G.** (1979) The great transgressions of the Late Cretaceous. *J. Geol. Soc. London*, **136**, 175–186.

Hetzel, A., **Böttcher, M.E.**, **Wortmann, U.G.** and **Brumsack, H.-J.** (2009) Paleo-redox conditions during OAE 2 reflected in Demerara Rise sediment geochemistry (ODP Leg 207). *Palaeogeogr. Palaeoclimatol. Palaeoecol.*, **273**, 302–328.

Higgins, M.B., **Robinson, R.S.**, **Husson, J.M.**, **Carter, S.J.** and **Pearson, A.** (2012) Dominant eukaryotic export production during ocean anoxic events reflects the importance of recycled NH_4^+. *Proc. Natl Acad. Sci. USA*, **109**, 2269–2274.

Holbourn, A. and **Kuhnt, W.** (2002) Cenomanian-Turonian palaeoceanographic change on the Kergulen Plateau: a comparison with Northern Hemisphere records. *Cretaceous Res.*, **23**, 333–349.

Hutton, A.C. (1987) Petrographic classification of oil shales. *Int. J. Coal Geol.*, **8**, 203–231.

Jarvis, I., **Gale, A.S.**, **Jenkyns, H.C.** and **Pearce, M.A.** (2006) Secular variation in Late Cretaceous carbon isotopes: a new $\delta^{13}C$ carbonate reference curve for the Cenomanian-Campanian (99.6–70.6 Ma). *Geol. Mag.*, **143**, 561–608.

Jarvis, I., **Lignum, J.S.**, **Gröcke, D.R.**, **Jenkyns, H.C.** and **Pearce, M.A.** (2011) Black shale deposition, atmospheric CO2 drawdown, and cooling during the Cenomanian-Turonian Oceanic Anoxic Event. *Paleoceanography*, **26**, PA3201. doi:10.1029/2010PA002081.

Jenkyns, H.C. (2003) Evidence for rapid climate change in the Mesozoic–Palaeogene greenhouse world. *Phil. Trans. Roy. Soc. London A*, **361**, 1885–1916.

Jenkyns, H.C. (2010) Geochemistry of oceanic anoxic events. *Geochem. Geophys. Geosyst.*, **11**, Q03004. doi:10.1029/2009GC002788.

Keller, G. and **Pardo, A.** (2004) Age and paleoenvironment of the Cenomanian-Turonian global stratotype section and point at Pueblo, Colorado. *Mar. Micropaleontol.*, **51**, 95–128.

Kennedy, W.F., **Walaszczyk, I.** and **Cobban, W.A.** (2005) The global boundary Stratotype section and point for the base of the Turonian Stage of the Cretaceous: Pueblo, Colorado, USA. *Episodes*, **28**, 93–104.

Kerr, A.C. (1998) Oceanic plateau formation: a cause of mass extinction and black shale deposition around the Cenomanian-Turonian boundary? *J. Geol. Soc. London*, **155**, 619–626.

Kolonic, S., **Wagner, T.**, **Forster, A.**, **Sinninghe Damsté, J.S.**, **Walsworth-Bell, B.**, **Erba, E.**, **Turgeon, S.**, **Brumsack, H.-J.**, **Chellai, E.-H.**, **Tsikos, H.**, **Kuhnt, W.** and **Kuypers, M.M.M.** (2005) Black shale deposition on the northwest African shelf during the Cenomanian-Turonian oceanic anoxic event: climate coupling and global organic-carbon burial. *Paleoceanography*, **20**, PA1006. doi:10.1029/2003PA000950.

Kuypers, M.M.M., **Lourens, L.J.**, **Rijpstra, W.I.C.**, **Pancost, R.D.**, **Nijenhuis, I.A.** and **Sinninghe Damsté, J.S.** (2004) Orbital forcing of organic carbon burial in the proto-North Atlantic during oceanic anoxic event 2. *Earth Planet. Sci. Lett.*, **228**, 465–482.

Larson, R.L. and **Erba, E.** (1999) Onset of the mid-Cretaceous greenhouse in the Barremian-Aptian: igneous events and the biological, sedimentary, and geochemical responses. *Paleoceanography*, **14**, 663–678.

Lees, J.A. (2007) New and rarely reported calcareous nannofossils from the Late Cretaceous of coastal Tanzania: outcrop samples and Tanzania Drilling Project Sites 5, 9 and 15. *J. Nannopl. Res.*, **29**, 39–65.

Lenniger, M., **Nøhr-Hansen, H.**, **Hills, L.V.** and **Bjerrum, C.J.** (2014) Arctic black shale formation during Cretaceous Oceanic Anoxic Event 2. *Geology*, **42**, 799–802.

Meyers, P.A., **Yum, J.-G.** and **Wise, S.W.** (2009) Origins and maturity of organic matter in mid-Cretaceous black shales from ODP Site 1138 on the Kerguelen Plateau. *Mar. Petrol. Geol.*, **26**, 909–915.

Meyers, S.R., **Sageman, B.B.** and **Arthur, M.A.** (2012) Obliquity forcing of organic matter accumulation during Oceanic Anoxic Event 2. *Paleoceanography*, **27**, PA3212. doi:10.1029/2012PA002286.

Meyers, S.R., **Sageman, B.B.** and **Hinnov, L.A.** (2001) Integrated quantitative stratigraphy of the Cenomanian-Turonian Bridge Creek Limestone member using evolutive harmonic analysis and stratigraphic modeling. *J. Sed. Res.*, **71**, 627–643.

Mohr, B.A.R., **Wähnert, V.** and **Lazarus, D.** (2002) Mid-Cretaceous paleobotany and palynology of the Central Kerguelen Plateau, Southern Indian Ocean (ODP Leg 183, Site 1138). *Proc. ODP Sci. Results* (Eds F.A. Frey, M.F. Coffin, P.J. Wallace and P.G. Quilty), **183**, 1–39. doi:10.2973/odp.proc.sr.183.008.2002.

Mort, H.P., **Adatte, T.**, **Föllmi, K.B.**, **Keller, G.**, **Steinmann, P.**, **Matera, V.**, **Berner, Z.** and **Stüben, D.** (2007) Phosphorus and the roles of productivity and nutrient recycling during oceanic anoxic event 2. *Geology*, **35**, 483–486.

Monechi, S. and **Thierstein, H.** (1985) Late Cretaceous-Eocene nannofossil and magnetostratigraphic correlations near Gubbio, Italy. *Mar. Micropaleontol.*, **9**, 419–440.

Monteiro, F.M., **Pancost, R.D.**, **Ridgwell, A.** and **Donnadieu, Y.** (2012) Nutrients as the dominant control of anoxia and euxinia across the Cenomanian-Turonian oceanic anoxic event (OAE-2): model-data comparison. *Paleoceanography*, **27**, PA4209. doi:10.1029/2012PA002351.

Montoyo-Pina, C., **Weyer, S.**, **Anbar, A.D.**, **Pross, J.**, **Oschmann, W.**, **van de Schootbrugge, B.** and **Arz, H.W.** (2010) Global enhancement of ocean anoxia during Oceanic Anoxic Event 2: a quantitative approach using U isotopes. *Geology*, **38**, 315–318.

Nägler, T.F., **Anbar, A.D.**, **Archer, C.**, **Goldberg, T.**, **Gordon, G.W.**, **Greber, N.D.**, **Siebert, C.**, **Sohrin, Y.** and **Vance, D.** (2014) Proposal for an international molybdenum isotope measurement standard and data representation. *Geostand. Geoanal. Res.*, **38**, 149–151.

Nägler, T.F., **Neubert, N.**, **Böttcher, M.E.**, **Dellwig, O.** and **Schnetger, B.** (2011) Molybdenum isotope fractionation in pelagic euxinia: evidence from the modern Black and Baltic Seas. *Chem. Geol.*, **289**, 1–11.

Neal, C.R., **Mahoney, J.J.** and **Chazey, W.J., III** (2002) Mantle sources and the highly variable role of continental lithosphere in basalt petrogenesis of the Kerguelen Plateau and Broken Ridge LIP: results from ODP Leg 183. *J. Petrol.*, **43**, 1177–1205.

Nesbitt, H.W. and **Young, G.M.** (1982) Early Proterozoic climates and plate motions inferred from major element chemistry of lutites. *Nature*, **299**, 715–717.

Odin, G.S. and **Matter, A.** (1981) De glauconiarum origine. *Sedimentology*, **28**, 611–641.

Owens, J.D., **Gill, B.C.**, **Jenkyns, H.C.**, **Bates, S.M.**, **Severmann, S.**, **Kuypers, M.M.M.**, **Woodfine, R.G.** and **Lyons, T.W.** (2013) Sulfur isotopes track the global extent and dynamics of euxinia during Cretaceous Oceanic Anoxic Event 2. *Proc. Natl Acad. Sci. USA*, **110**, 18407–18412.

Parente, M., **Frijia, G.**, **Di Lucia, M.**, **Jenkyns, H.C.**, **Woodfine, R.G.** and **Baroncini, F.** (2008) Stepwise extinction of larger foraminifera at the Cenomanian-Turonian boundary: a shallow water perspective on nutrient fluctuations during Oceanic Anoxic Event 2 (Bonarelli Event). *Geology*, **36**, 715–718.

Paul, C.R.C., **Lamolda, M.A.**, **Mitchell, S.F.**, **Vaziri, M.R.**, **Gorostido, A.** and **Marshall, J.D.** (1999) The Cenomanian-

Turonian boundary at Eastbourne (Sussex, UK): a proposed European reference section. *Palaeogeogr. Palaeoclimatol. Palaeoecol.*, **150**, 83–121.

Perch-Nielsen, K. (1985) Mesozoic calcareous nannofossils. In: *Plankton Stratigraphy* (Eds H.M. Bolli, J.B. Saunders and K. Perch-Nielsen), pp. 329–427. Cambridge University Press, Cambridge.

Pilipchuk, M.F. and **Volkov, I.I.** (1974) Behavior of molybdenum in processes of sediment formation and diagenesis in Black Sea: geochemistry. In: *The Black Sea – Geology, Chemistry and Biology* (Ed. E.T. Degens and D.A. Ross), *AAPG Mem.*, **20**, 542–553. Tulsa, USA.

Pistiner, J.S. and **Henderson, G.M.** (2003) Lithium-isotope fractionation during continental weathering processes. *Earth Planet. Sci. Lett.*, **214**, 327–339.

Pogge van Strandmann, P.A.E., **Burton, K.W.**, **James, R.H.**, **van Calsteren, P.**, **Gíslason, S.R.** and **Mokadem, F.** (2006) Riverine behaviour of uranium and lithium isotopes in an actively glaciated basaltic terrain. *Earth Planet. Sci. Lett.*, **251**, 134–147.

Pogge van Strandmann, P.A.E., **Jenkyns, H.C.** and **Woodfine, R.G.** (2013) Lithium isotope evidence for enhanced weathering during Oceanic Anoxic Event 2. *Nat. Geosci.*, **6**, 668–672.

Poulton, S.W., **Henkel, S.**, **März, C.**, **Urquhart, H.**, **Flögel, S.**, **Kasten, S.**, **Sinninghe Damsté, J.S.** and **Wagner, T.** (2015) A continental-weathering control on orbitally driven redox-nutrient cycling during Cretaceous Oceanic Anoxic Event 2. *Geology*, **43**, 963–966.

Pratt, L.M. and **Threlkeld, C.N.** (1984) Stratigraphic significance of $^{13}C/^{12}C$ ratios in mid-Cretaceous rocks of the Western Interior, U.S.A. In: *Mesozoic of Middle North America* (Eds D.F. Stott and D.J. Glass), *Bull. Can. Soc. Petrol. Mem.*, **9**, 305–312.

Rudnick, R.L. and **Gao, S.** (2003) Composition of the continental crust. In: *Treatise on Geochemistry* (Eds D.H. Heinrich and K.T. Karl), pp. 1–64. Pergamon, Oxford, U.K..

Sageman, B.B., **Meyers, S.R.** and **Arthur, M.A.** (2006) Orbital time scale and new C-isotope record for the Cenomanian-Turonian boundary stratotype. *Geology*, **34**, 125–128.

Schlanger, S.O. and **Jenkyns, H.C.** (1976) Cretaceous oceanic anoxic events: causes and consequences. *Geol. Mijnbouw*, **55**, 179–184.

Scholle, P.A. and **Arthur, M.A.** (1980) Carbon isotope fluctuations in Cretaceous pelagic limestones: potential stratigraphic and petroleum exploration tool. *AAPG Bull.*, **64**, 67–87.

Shipboard Scientific Party (2000) Site 1138. In: *Proc. ODP, Init. Repts. 183* (Eds M.F. Coffin, F.A. Frey, P.J. Wallace, *et al.*), pp. 1–205. Ocean Drilling Program, College Station, TX.

Sissingh, W. (1977) Biostratigraphy of Cretaceous calcareous nannoplankton. *Geol. Mijnbouw*, **56**, 37–65.

Taylor, G.H., **Teichmüller, M.**, **Davies, A.**, **Diessel, C.F.K.**, **Littke, R.** and **Robert, P.** (1998) *Organic Petrology*. Gehrüder Borntraefer, Berlin, Stuttgart.

Thurow, J., **Brumsack, H.-J.**, **Rullkötter, J.**, **Littke, R.** and **Meyers, P.** (1992) The Cenomanian-Turonian Boundary event in the Indian Ocean – a key to understand the global picture. In: *Synthesis of Results from Scientific Drilling in the Indian Ocean:* (Eds R.A. Duncan, D.K. Rea, R.B. Kidd, von Rad U. and J.K. Weissel), *AGU Geophys. Monogr.*, **70**, 253–274. American Geophysical Union, Washington, DC.

Tribovillard, N., **Algeo, T.J.**, **Lyons, T.** and **Riboulleau, A.** (2006) Trace metals as paleoredox and paleoproductivity proxies: an update. *Chem. Geol.*, **232**, 12–32.

Tribovillard, N., **Algeo, T.J.**, **Baudin, F.** and **Riboulleau, A.** (2011) Analysis of marine environmental conditions based on molybdenum-uranium covariation – applications to Mesozoic stratigraphy. *Chem. Geol.*, **324–325**, 46–58.

Tsikos, H., **Jenkyns, H.C.**, **Walsworth-Bell, B.**, **Petrizzo, M.R.**, **Forster, A.**, **Kolonic, S.**, **Erba, E.**, **Premoli Silva, I.**, **Wagner, T.** and **Sinninghe Damsté, J.S.** (2004) Carbon isotope stratigraphy recorded by the Cenomanian–Turonian Oceanic Anoxic Event: correlation and implications based on three key localities. *J. Geol. Soc. London*, **161**, 711–719.

Turgeon, S. and **Brumsack, H.-J.** (2006) Anoxic vs dysoxic events reflected in sediment geochemistry during the Cenomanian–Turonian Boundary Event (Cretaceous) in the Umbria–Marche Basin of central Italy. *Chem. Geol.*, **234**, 321–339.

Turgeon, S.C. and **Creaser, R.A.** (2008) Cretaceous oceanic anoxic event 2 triggered by a massive magmatic episode. *Nature*, **454**, 323–326.

van Bentum, E.C., **Reichart, G.-J.** and **Sinninghe-Damsté, J.S.** (2012) Organic matter provenance, palaeoproductivity and bottom water anoxia during the Cenomanian/Turonian oceanic anoxic event in the Newfoundland Basin (northern proto North Atlantic Ocean). *Org. Geochem.*, **50**, 11–18.

van Helmond, N.A.G.M., **Baroni, I.R.**, **Sluijs, A.**, **Damsté, S.** and **Slomp, C.P.** (2014) Spatial extent and degree of oxygen depletion in the deep proto-North Atlantic basin during Oceanic Anoxic Event 2. *Geochem. Geophys. Geosyst.*, **15**, 4254–4266.

Voigt, S., **Erbacher, J.**, **Mutterlose, J.**, **Weiss, W.**, **Westerhold, T.**, **Wiese, F.**, **Wilmsen, M.** and **Wonik, T.** (2008) The Cenomanian-Turonian of the Wunstorf section – (North Germany): global stratigraphic reference section and new orbital time scale for Oceanic Anoxic Event 2. *Newsl. Stratigr.*, **43**, 65–89.

Westermann, S., **Vance, D.**, **Cameron, V.**, **Archer, C.** and **Robinson, S.A.** (2014) Heterogeneous oxygenation states in the Atlantic and Tethys oceans during Oceanic Anoxic Event 2. *Earth Planet. Sci. Lett.*, **404**, 178–189.

Manuscript received 16 December 2015; revision accepted 13 June 2016